

# An End-to-End Multi-Stage Kill-Chain Attack on Quantum Neural Networks: Demonstration on Trapped-Ion Hardware

Cedric Brüggemann\*, Daniel Herr\*, Daniel Ohl de Mello\*, Pascal Debus†, Maximilian Wendlinger†, Kilian Tscharke†, Juris Ulmanis‡, Alexander Erhard‡, Arthur Schmidt§, Fabian Petsch§  
\*d-fine GmbH, Frankfurt, Germany

†Fraunhofer Institute for Applied and Integrated Security (AISEC), Garching near Munich, Germany

‡Alpine Quantum Technologies (AQT) GmbH, Innsbruck, Austria

§Federal Office for Information Security (BSI), Bonn, Germany

**Abstract**—We demonstrate an end-to-end, multi-stage attack against a quantum neural network (QNN) model that is executed on a trapped-ion quantum computer. Our chain combines side-channel reconnaissance, crosstalk characterization, adversarial example generation, and a physical crosstalk attack that realizes the adversarial perturbation on the device. We cover the full attack chain on ion traps and report the corresponding superconducting-hardware experiments in the appendix. We discuss implications for QaaS providers and hardware mitigations.

**Index Terms**—Quantum machine learning, security, side-channel attacks, crosstalk, adversarial examples, trapped ions, superconducting qubits, kill-chain

## I. INTRODUCTION

Deployments of Quantum Machine Learning (QML) algorithms on real quantum processing units (QPUs) fundamentally expand the attack surface beyond what is captured by idealized or noise-augmented simulations. Existing work on the security of QML has primarily examined individual attack vectors in isolation. While these results provide valuable insights into specific vulnerabilities, they do not capture how an adversary may combine multiple techniques into a coherent attack campaign. In practical deployment scenarios, especially in cloud-based and multi-tenant settings, attacks are rarely executed as isolated events. Instead, information gained during reconnaissance can be used to reduce uncertainty in subsequent stages, enabling targeted manipulations. Building on an extensive review of the literature, we develop a structured taxonomy of QML attack vectors and align them with the respective stages of a quantum-aware kill chain, following the spirit of the MITRE ATLAS framework for classical ML [4]. This framework makes explicit the interdependencies between different threat classes, spanning hardware-level weaknesses (e.g., side-channel leakage and crosstalk-induced faults), data and algorithm manipulation (e.g., poisoning and circuit backdoors), as well as privacy-focused attacks (e.g., model extraction and training data inference). By systematically evaluating these interdependencies, our approach facilitates the design of proactive and integrated defense-in-depth strategies. One of the findings of this kill chain perspective is the possibility of linked

multi-stage attacks, where the attacker uses side-channel attacks to perform reconnaissance and learn as much as possible about a victim machine learning model, and then use this information to fine-tune attacks, e.g., based on noise injection, to attack a model. Importantly, all evaluated attack vectors operate within the constraints of current noisy intermediate-scale quantum (NISQ) devices and do not rely on fault-tolerant assumptions, making them directly relevant for near-term quantum machine learning deployments. The remainder of this paper is organized as follows. Section II summarizes related work, positioning our contributions within the existing literature. Section III introduces the necessary background, covering both the theoretical foundations and the hardware-specific aspects. Section IV details the experimental pipeline, experimental setup, and attack methodologies employed in this study. Next, we present the results in Section V. These findings are subsequently interpreted and critically assessed in the discussion section VI, where defensive strategies against the attack vectors are also discussed. Finally, in Section VII, we summarize the main contributions.

## II. RELATED WORK

### A. Side-Channel Attacks on Quantum Computers

One of the main targets of side-channel attacks (SCA) is reverse engineering of the quantum circuit. SCA based on power traces, which can be calculated directly from the control electronics or the pulse program, have already been described in the literature [6, 24]. In addition, timing-based approaches have been proposed in [14] and successfully tested on IBM quantum computing hardware. Studies exploiting crosstalk as a side channel have also been reported [3, 12]. However, all of these attacks were executed on superconducting devices, whereas our work focuses on trapped-ion platforms as well.

### B. Adversarial Attacks on QML

Adversarial evasion attacks are characterized by the fact that they deliberately but minimally perturb the input of a (QML) model to achieve an incorrect classification by the model.

A variety of different attacks have been researched in the classical case, and the vulnerability of QML methods was established (in theory) early on by Ref. [13]. In empirical studies, vulnerability to standard white box methods (Fast Gradient Sign Method [9], Projected Gradient Descent [16]) was shown in various works in simulation [15] and also on real quantum hardware [20] for both classical and quantum data. Simple defenses such as adversarial training, showing improved robustness under adversarial attack [5]. Ref. [23] also investigates transfer attacks as gray-box/black-box methods and suggests a possible quantum advantage in robustness. Adversarial robustness, as well as the influence of data encoding and advanced defense mechanisms such as Lipschitz regularization, was further investigated by [22] and led to some limitations of this quantum advantage claim.

### C. Physical Fault Injection & Crosstalk

Beyond side-channel information leakage, crosstalk can also be exploited as a noise attack to deliberately disrupt quantum computations. In this context, [8] propose explicit crosstalk-based attacks on trapped-ion quantum computers, where adversarial circuits inject sequences of entangling gates, primarily CNOT operations, to amplify crosstalk effects in a multi-tenant setting. The effectiveness of these attacks is demonstrated using noise-based emulation of trapped-ion devices. In superconducting architectures, noise can be deliberately induced through CNOT drives applied to neighboring qubits [1, 10] or by exploiting SWAP paths [12].

### D. Multi-Stage Attacks and Kill-Chains

In classical IT security, attacks are rarely executed as isolated actions but rather unfold as structured, multi-stage campaigns. Kill-chain models capture this progression by decomposing adversarial behavior into sequential phases. Prominent examples are the Lockheed Martin Cyber Kill Chain<sup>1</sup> and the MITRE ATT&CK framework<sup>2</sup>, which provide a systematic vocabulary for describing attacker objectives, capabilities, and techniques across different stages. A key insight of kill-chain thinking is that early-stage actions often serve as prerequisites for later, higher-impact attacks: information gathered during reconnaissance can enable precise exploitation, while partial access gained early may be leveraged to establish persistence or execute targeted manipulation. As argued in our prior work [4], this perspective is particularly relevant for quantum machine learning systems deployed in cloud-based, multi-tenant environments, where physical-layer effects, control software, and algorithmic components interact in non-trivial ways. Adapting classical kill-chain models to the QML context enables structured reasoning about how side-channel leakage, crosstalk, noise injection, and model manipulation can be combined into multi-stage attack scenarios, rather than being analyzed in isolation.

<sup>1</sup><https://www.lockheedmartin.com/en-us/capabilities/cyber/cyber-kill-chain.html>

<sup>2</sup><https://attack.mitre.org/>

### A. Kill-Chain Model for QML

Drawing on classical kill chain frameworks, we adapt a five-stage model to accommodate the unique architecture and life-cycle of quantum machine learning. These stages, namely Reconnaissance, Initial Access, Model Access / Manipulation, Persistence, and Exfiltration / Impact, cover the necessary steps from an adversary's early information gathering to the final destructive or exfiltrative actions.

- **Reconnaissance stage** The reconnaissance phase includes general discovery techniques as well as quantum-specific methods for understanding circuit structure and resource usage. In classical IT systems, reconnaissance usually involves scanning for open ports or unpatched services. In contrast, QML contexts present more subtle approaches, such as power or timing side-channels, which can disclose information about circuit structure.
- **Initial Access stage:** After the attacker finds a viable entry point, they proceed to the initial access stage, where they establish partial yet significant footholds. This access may involve manipulating scheduling algorithms that assign jobs for securing concurrent execution with victim circuits on a cloud quantum device, or injecting malicious data into a shared dataset.
- **Model Access / Manipulation stage:** Once a foothold is established, this stage signifies a shift to actively engaging with the victim's QML model or related circuits. An adversary could alter parameterized gates to reduce accuracy, embed hidden trojans in the transpiled circuit, or introduce extra noise during training. Such manipulation can occur throughout the iterative training loop, particularly in variational circuits, and may remain stealthy if the malicious behavior is triggered only under specific inputs, circuit configurations, or training conditions.
- **Persistence stage:** Depending on their overall objective, an attacker may attempt to establish stealthy long-term control mechanisms within the system or the victim model. The most straightforward example of this is Trojan attacks through data poisoning, but other options, such as intentional miscalibration for gate injection, could also be feasible.
- **Exfiltration / Impact:** Ultimately, the final stages represent the culmination of the adversary's goals. In some instances, exfiltration involves stealing quantum model parameters or measurement data, thereby replicating proprietary QML logic without compensating for the model's development. In other cases, the main objective is sabotage, such as inducing misclassifications, creating DoS conditions through amplified noise, or exposing private data used in training. This concluding stage highlights that, while multi-stage attacks can occur at any point, the attacker's primary aim is usually achieved when they either exfiltrate sensitive assets (e.g., trained QML models, confidential data) or cause disruptive effects (e.g., inference failures).

For a more detailed discussion of this kill-chain model, we refer the reader to prior work [4].

## B. QML Preliminaries

1) *Architectures*: In this work we focus on variational classifiers, that is, parameterized quantum circuits for supervised classification tasks, where classical input data are encoded into qubit states, processed through variational layers with trainable parameters, and measured to predict discrete class labels. Upon measurement, the circuit’s outputs feed back into a classical optimizer, such as gradient descent, to refine those same parameters over multiple iterations. To place this concrete choice within the broader design space of quantum machine learning, we adopt the view summarized in Table I.

TABLE I  
HIERARCHY OF QML MODEL COMPONENTS.

Category	Illustrative subcategories
QML NISQ Architecture Types	Variational Classifier Autoencoder Kernel Methods Tensor Network Ansatz
Architectural Variations	Sequential Re uploading with Separate Layers Re uploading with Integrated Layers
Data Encoding Strategies	Angle Encoding Amplitude Encoding Basis Encoding
Layer Types	Basic Entangling Layers Strongly Entangling Layers IQP Ansatz
Entangling Gate Details	Gate Types Entanglement Patterns (Cyclic, Range based)
Rotations	Rotation Axis / Pauli Generator Rotation Angles (and Precision)

At the top level, we distinguish between different QML NISQ architecture types (variational classifiers, autoencoders, kernel based models, and tensor network inspired ansatzes), which define the overall learning paradigm and circuit structure. Architectural variations specify how data encoding and trainable layers are arranged (purely sequential or with different forms of data re uploading), while data encoding strategies determine how classical features are mapped to quantum states, with direct consequences for circuit depth and width. Layer types control the expressive power and entanglement structure of the repeated building blocks, from basic entangling layers to strongly entangling ones and Instantaneous Quantum Polynomial (IQP) style ansatzes. Finally, entangling gate details (specific two-qubit gate choices and entanglement patterns) together with the choice of rotation generators and angles specify the concrete low level implementation. This illustrates that for a fixed learning task there exists a very large number of possible designs.

2) *Data Encoding & Reuploading*: The performance of a QML model on classical data is heavily dependent on the chosen feature map [19]. This choice represents a trade-off between qubit resources, circuit depth, and the amount of information encoded. Some techniques for mapping classical

input data onto quantum states, affecting circuit depth, width, and learning ability [21] are:

- **Angle Encoding**: Features are translated into rotation angles for single-qubit gates. This approach is simple and hardware-compatible.
- **Amplitude Encoding**: Data are encoded into the amplitudes of a quantum state. While compact in terms of required qubits, this method requires complex state preparation.
- **Basis Encoding**: Features are mapped to distinct computational basis states, making this encoding suitable for discrete data.

The data encoding scheme used in this work is the so-called reupload encoding introduced by Perez-Salinas et al. [18], where the features of the input vector are grouped into tuples and sequentially inserted as rotational angles of (general) rotational gates. The details are covered in Section IV-B.

## C. Power Traces

Quantum computers implement gate operations via control pulses. For example, superconducting devices use microwave pulses [6], while AQT trapped-ion systems employ laser pulses. Since these control pulses are generated by classical hardware, they can be intercepted, allowing an attacker to deduce critical circuit details. A central property of quantum hardware is its set of native (or basis) gates, which varies across manufacturers and devices. Before execution, high-level quantum circuits are decomposed into these basis gates. This process, analogous to classical compilation, involves transpiling the circuit at the gate level by breaking down non-native gates into native ones, optimizing the circuit, mapping logical qubits to physical qubits, and finally scheduling the resulting pulses. The final pulse-level circuit description specifies all necessary pulses, including their envelopes, frequencies, phases, and precise timing to ensure the circuit operates correctly on the target quantum device. The attacker aims to uncover quantum circuit details from captured power traces.

## D. Crosstalk Mechanisms

Quantum crosstalk refers to unintended interactions between qubits in a quantum processor. These interactions allow operations on one set of qubits to influence nearby qubits, thereby reducing fidelity and introducing errors that degrade computational performance [17].

1) *Ion-Trap Crosstalk*: In trapped ion devices quantum gates are implemented using tightly focused laser beams that address individual ions. Each beam generates a localized electric field profile centered on its target ion but with a finite spillover onto neighboring sites due to the diffraction limit. This spatial profile implies that single qubit gates introduce nearest neighbor crosstalk because their beams produce the largest off target fields. In contrast, two qubit gates realized via frequency-detuned laser interactions exhibit strongly suppressed crosstalk since the detuning reduces unwanted excitation of non-addressed ions.

2) *Superconducting Crosstalk*: In superconducting transmon processors, crosstalk arises from unintended interactions induced by microwave control pulses in the presence of frequency crowding and residual couplings between neighboring qubits. In fixed-frequency architectures, collisions between qubit transition frequencies and anharmonic transitions can lead to undesired driving of individual qubits or induce spurious interactions during single- and two-qubit gate operations, thereby degrading computational fidelity [11]. In particular, two-qubit gates constitute a major source of crosstalk in superconducting devices, in contrast to AQT trapped-ion systems, where crosstalk is predominantly driven by imperfect single-qubit addressing.

### E. Adversarial Examples

Adversarial examples in (quantum) machine learning are small, often imperceptible perturbations  $\delta$ , typically constrained by  $\|\delta\|_\infty \leq \epsilon$ , that are crafted to induce misclassification by maximizing the model’s loss:

$$\delta^* = \arg \max_{\|\delta\|_\infty \leq \epsilon} \mathcal{L}(f(x + \delta; \theta), y).$$

Here,  $\mathcal{L}(f(x; \theta), y)$  denotes the loss function measuring the discrepancy between the model’s prediction  $f(x; \theta)$  and the true label  $y$ , and  $x$  is the original input sample. In practice, this optimization is often approximated using Projected Gradient Descent (PGD), which iteratively increases the loss with respect to the input by taking gradient-ascent steps and then projects the perturbed sample back onto the  $\ell_\infty$  ball of radius  $\epsilon$  centered at the original input. Formally, the PGD update takes the form

$$x^{(t+1)} = \text{Proj}_{\|\cdot\|_\infty \leq \epsilon} \left[ x^{(t)} + \alpha \cdot \text{sign}(\nabla_x \mathcal{L}(f(x^{(t)}), y)) \right],$$

where  $\alpha$  is the step size. Both classical convolutional networks and variational quantum circuits (employing re-upload or amplitude encodings) have been shown to succumb to such attacks, revealing shared vulnerabilities between QML and classical models [22].

### F. Threat Model

One aspect that is often neglected in current literature on adversarial QML, but is an established process in classic IT security, is threat modeling. A threat model that explains typical threat scenarios and assesses the potential impact according to the attacker’s capabilities and resources, should be part of any analysis of security aspects of QML.

1) *Attacker Capabilities*: Since we perform different experiments, the attacker’s capabilities must be considered individually for each attack scenario. Table II summarizes the required access levels and assumptions.

2) *Attack Goals*: The goal of the **power trace attack** is to extract as much information as possible about the victim circuit, such as the number of involved qubits, the executed gate sequence, or the trained parameters of the victim model. The goal of **adversarial attacks** is to deliberately manipulate the input of a model with minimal perturbations

TABLE II  
ATTACKER CAPABILITIES AND ASSUMPTIONS FOR THE EVALUATED  
ATTACK SCENARIOS.

Attack Vector	Required Access and Assumptions
Power Trace Attack	Requires access to fine-grained analogue power information at the control-electronics layer of a device. Such access is not available to ordinary cloud users but represents a realistic threat model for privileged insiders, on-premise deployments, or future platforms exposing pulse-level diagnostics.
Adversarial Attacks via Data Poisoning	Assumes white-box access to model gradients and the ability to repeatedly query the trained QNN during iterative PGD optimisation. No structural or hardware-level information is required. The primary computational cost arises from repeated forward and backward passes.
Adversarial Examples via Crosstalk	Requires white-box gradient access and repeated query capability, in addition to a multi-tenant execution scenario that enables concurrent circuit execution and the exploitation of crosstalk effects during the execution of the victim circuit. Furthermore, explicit timing information about the victim circuit is required, as the attacker’s gates must be executed at specific positions during the circuit execution.

such that the model produces incorrect predictions or misclassifications, without modifying the model parameters or the underlying hardware. The goal of **adversarial examples via crosstalk** is to physically induce adversarial perturbations through crosstalk, such that concurrent attacker-controlled gate executions distort the effective input seen by the victim model and approximate the effect of analytically computed adversarial examples, without modifying the input data.

## IV. METHODS

### A. Overall Experimental Pipeline

Our experimental methodology follows a deliberately chained, multi-stage attack pipeline that mirrors an adversarial workflow against a deployed QNN. The central objective is to demonstrate how information obtained during an initial reconnaissance phase can be exploited to enable a targeted manipulation of a victim QNN via hardware-induced crosstalk. In the first stage, the attacker performs *side-channel reconnaissance* to infer structural properties of the victim QNN. In this work, we demonstrate reconnaissance through a power-trace-based analysis. By comparing the observed signatures of the victim QNN against a library of benchmark circuits, the attacker is able to infer key architectural parameters such as the number of qubits, circuit depth, and entangling structure. Crucially, this stage yields an approximate temporal map of the victim circuit execution, allowing the attacker to identify when specific data-encoding rotations are executed. Building on this knowledge, the second stage focuses on the construction of adversarial examples. We first generate conventional adversarial examples using gradient-based methods on the victim model that matches the inferred architecture of the victim QNN.

However, physical constraints of the hardware significantly restrict how such perturbations can be realized in practice. In particular, on the considered AQT trapped-ion platform, crosstalk effects can be reliably induced only through single-qubit rotations. Since virtual  $R_Z$  gates do not induce any physical disturbance, as a consequence, only input features encoded via  $R_Y$  rotations can be perturbed by crosstalk. We therefore refine the adversarial generation process by explicitly constraining perturbations to the subspace corresponding to  $R_Y$ -encoded inputs, resulting in *adversarial examples via crosstalk* that respect the hardware constraints of the device. In the final stage, the attack is executed on real quantum hardware. Using the timing information obtained during reconnaissance, the attacker schedules carefully chosen disturbance operations on neighboring qubits at specific points in time during the execution of the victim QNN. These operations induce controlled crosstalk, with the goal to approximate the previously constructed adversarial perturbations, thereby manipulating the effective input seen by the victim model.

### B. Victim QNN Design

In this section, we introduce the victim QNN, which serves as the target of our attacks detailed in our experimentation plan, and define the benchmark circuits used in the considered attacks. The victim QNN is a modification of the QNN introduced in [22]. In the latter implementation, the input features of the QNN are incorporated as rotational angles in the circuit. The QNN’s classification task involves assigning each input image to its respective class. Notably, the dataset depicted in fig. 1 comprises four distinct classes:  $\{+, -, \vdash, \dashv\}$ .

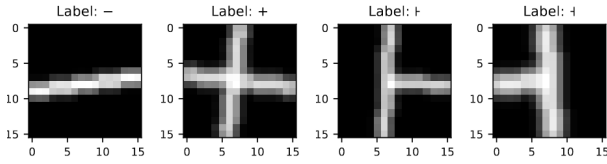


Fig. 1. An overview of the used dataset [22]. Shown are examples from the individual classes of the dataset.

For an input image of dimensions  $16 \times 16 = 256$ , the quantum circuit uses 8 qubits and  $L = 32$  layers. Each layer consists of a block of rotational gates (whose angles are determined by grouped 3-tuples of input features) followed by an entangling layer, which yields a total of

$$32 \cdot 8 \cdot 3 = 768$$

variational parameters. Moreover, each of these 768 rotation parameters has a corresponding input encoding weight, doubling the total number of trainable parameters, leading to a total of 1536 trainable parameters in the model.

The data encoding scheme used is the so-called re-upload encoding introduced by Perez-Salinas et al. [18]. Given some input 3-tuple  $x$  and weights  $w, \theta \in \mathbb{R}^3$ , this general rotation can be written as a product of unitaries

$$R(wx + \theta) = U_{w,\theta}(x) = \prod_{j=1}^3 e^{-i(w_j x_j + \theta_j) H_j},$$

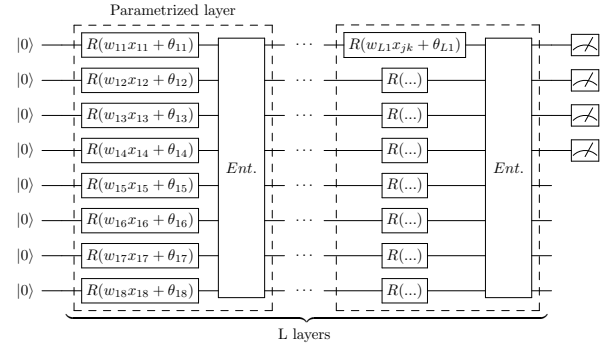


Fig. 2. A conceptual overview of the re-upload encoding architecture from reference [22].

where the typical gate decomposition of general rotational gates employs the Hamiltonians

$$H_1 = \frac{1}{2}\sigma_Z, \quad H_2 = \frac{1}{2}\sigma_Y, \quad H_3 = \frac{1}{2}\sigma_Z.$$

For re-uploading, this implies that each feature of a  $D = 256$ -dimensional input sample is presented to the model three times. This choice is motivated by the inherent flexibility of the re-uploading paradigm: it decouples the number of qubits from the input dimension, thereby allowing high-dimensional inputs to be encoded repeatedly onto a fixed number of qubits. As model output, a four-dimensional vector is produced by computing the expectation values of the Pauli  $Z$  operators on the first four qubits, each corresponding to one of the four target classes. These expectation values serve as the inputs to the  $\arg \max$  function, which is used to select the predicted class. The parameter  $r$  defines the entangling structure of the QNN. If  $r$  is not explicitly set (i.e., when  $r$  is specified as None), a default value is computed internally. Specifically, for the  $l$ th layer in a circuit with  $M$  wires, the value of  $r$  is determined as  $r = l \bmod M$ . Once this value is established, the entangling part of each layer is constructed by applying CNOT gates. For every qubit  $q$ , a CNOT gate is applied with qubit  $q$  acting as the control and qubit  $(q+r) \bmod M$  as the target. In situations where the modulo operation yields zero,  $r$  is adjusted and set to 1 to ensure a proper entanglement pattern.

We reduce the complexity of the model by applying Principal Component Analysis (PCA) to the  $16 \times 16$  pixel images, projecting them onto the top 16 principal components and reducing the number of qubits from eight to four. The re-uploading scheme is retained, and the optimized model is implemented with four strongly entangling layers (with  $r$  set to the default value), effectively corresponding to three re-uploads. Through this approach, the number of variational parameters drops from  $32 \times 8 \times 3 \times 2 = 1536$  to  $4 \times 4 \times 3 \times 2 = 96$ .

Similarly, as in the previous model, the output is derived by computing the expectation values of the individual Pauli  $Z$  operators for each of the four output qubits. These correspond directly to the four target classes.

For each input, the quantum circuit returns a four-dimensional vector of  $Z$  expectation values, one per output qubit. Classification is then performed by applying the  $\arg \max$  function to this vector, selecting the index with the highest value as the predicted class.

We trained the model using state vector simulation to optimize the rotation parameters. Across a total of 1000 training samples and 200 test samples, the model achieved a training accuracy of 0.885 and a test accuracy of 0.875. These results reflect an upper bound of accuracy that can be expected using real hardware.

To better understand the performance of the model for individual classes, we analyze the average highest and second highest expectation values predicted by the QNN for each label (see Fig. 3). Here, labels 0 and 2 correspond to the symbols "-" and "┌", while labels 1 and 3 represent "+" and "└" respectively.

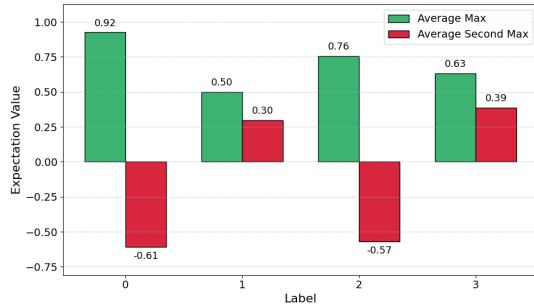


Fig. 3. Average highest and second highest Pauli- $Z$  expectation value (per true label) on the training set.

For samples with true labels 0 and 2, the model's average maximum expectation value is noticeably higher than for labels 1 and 3. At the same time, the average second highest expectation value for classes 1 and 3 is substantially higher than for 0 and 2. This result suggests that the quantum model is, on average, much more confident in its predictions for classes 0 and 2, whereas the model is often less decisive and more ambiguous for classes 1 and 3.

### C. Benchmark Circuits

The main goal of all presented stage one attacks is to infer the structure of a victim QNN by comparing its side-channel signature with those generated by a set of benchmark candidate circuits. For these circuits, no specific input data is provided. Instead, the rotational parameters of each candidate circuit are randomized uniformly between 0 and  $2\pi$ . In experiments where multiple samples are collected, the rotation angles of the benchmark circuits are re-randomized for each run of the victim QNN, ensuring that a robust and statistically representative side-channel signature is obtained for every candidate. By comparing the victim's measured side-channel signature with the signatures of the candidate circuits, the attack can identify the most likely underlying circuit structure. When constructing the benchmark circuits, note that the **constraints**,

namely qubit count and circuit depth, are dictated by the underlying quantum computing device.

- The number of qubits available on the device determines the maximum number of qubits  $q$  that can be used in the circuit.
- The coherence time of the quantum device influences the depth of the circuit. The lower the coherence time, the less deep the circuit should be, as error probabilities increase with circuit depth.

These constraints need to be considered when designing the benchmark candidates to ensure that the chosen parameters are feasible for the specific quantum computing architecture being used. We decided to employ the re-uploading scheme exclusively. To evaluate the side-channel signatures, we systematically vary three key parameters, resulting in a total of 24 distinct benchmark configurations:

- **Number of Qubits:** Configurations will be built using either 4 or 8 qubits.
- **Number of Layers:** Circuits will be implemented with 2, 4, 6, and 8 layers.
- **Entanglement Parameter  $r$ :** The parameter  $r$  will determine the target qubit in the entangling CNOT gates. We will vary  $r$  by selecting explicit values of 1 and 2, as well as by using the default setting.

### D. Simulation of AQT Power Traces

Since real power traces from hardware are not available, we simulate the power traces as follows. To model the power trace on an AQT device, we assign to each qubit  $i$  and qubit pair  $(i, j)$  an amplitude coefficient derived from the raw corrections  $\{a_i\}_{i=0}^{N-1} = \{1, -1, 2, 3, 0, -2, -3, 0, -4, 4\}$ , for  $N = 10$  qubits. We then define the single and two qubit scaling factors  $\alpha_i = 1 + \frac{a_i}{100}$  and  $\beta_{ij} = 10 + \frac{a_i + a_j}{10}$ , such that  $\alpha_i$  modulates pulses on qubit  $i$  and  $\beta_{ij}$  modulates cross-resonance pulses between qubits  $i$  and  $j$ . Each basis gate is represented by a single rectangular pulse of fixed duration followed by a  $2 \mu\text{s}$  idle, with amplitude determined by the appropriate coefficient:

- $R_Z$  (virtual  $R_Z$ ): no physical pulse ( $P = 0$ ).
- $R(\theta, \phi)$  (general rotation): one  $10 \mu\text{s}$  pulse of amplitude  $\alpha_i \theta / \pi$ , then a  $2 \mu\text{s}$  idle.
- $R_{XX}(\theta)$  (XX interaction): one  $200 \mu\text{s}$  pulse of amplitude  $\beta_{ij} \theta / \pi$ , then a  $2 \mu\text{s}$  idle.

Given a circuit, we construct the time-ordered trace  $\{(t_k, P_k)\}_{k=0}^K$  by first initializing  $t_0 = 0$ ,  $t_1 = 2 \mu\text{s}$ , and  $P_0 = P_1 = 0$ .

For each subsequent gate, we append four entries: two identical amplitude values to represent the start and end of the rectangular pulse, followed by two zeros for the fixed  $2 \mu\text{s}$  idle.

Concretely, since the pulse duration  $\Delta_{\text{pulse}}$  is  $10\ \mu\text{s}$  for single-qubit gates and  $200\ \mu\text{s}$  for two-qubit gates, then

$$P_k = P_{k+1} = \begin{cases} \alpha_i \frac{\theta}{\pi}, & \text{for an } R(\theta, \phi) \text{ on qubit } i, \\ \beta_{ij} \frac{\theta}{\pi}, & \text{for an } R_{XX}(\theta) \text{ on } (i, j), \end{cases}$$

$$t_{k+1} - t_k = \Delta_{\text{pulse}}.$$

and

$$P_{k+2} = P_{k+3} = 0, \quad t_{k+2} - t_{k+1} = 0\ \mu\text{s}, \quad t_{k+3} - t_{k+2} = 2\ \mu\text{s}.$$

The resulting step function

$$P(t) = P_k, \quad t_k \leq t < t_{k+1},$$

captures each gate’s amplitude and timing exactly as produced by the AQT power trace simulator.

### E. Adversarial Example Generation

In this work, we consider the following threat assumption. Rather than training a surrogate model, we assume white-box access to the victim QNN and directly generate adversarial examples using the trained model in an idealized state vector simulation. This allows us to isolate the effect of hardware-induced noise and implementation-specific deviations on the transferability of adversarial examples, without conflating these effects with surrogate model mismatch. We start with evaluating the robustness of the victim QNN defined in Section IV-B and systematically construct adversarial examples for every sample in the training set using PGD, as described in V-B. The procedure iterates over all training samples and searches for the minimum perturbation in  $\ell_\infty$ -norm that causes the QNN to change its classification relative to the prediction for the unperturbed input. This search is iterative: for each sample, the maximum perturbation  $\epsilon$  is increased in increments of 0.1 up to a maximum of 1.0, and the smallest  $\epsilon$  for which a prediction change occurs is recorded. The evaluation workflow is as follows:

- 1) For each sample  $x$  from the set of training data, the model’s predicted label is computed.
- 2) We initialize the perturbation size  $\epsilon = 0.1$  and iteratively apply the PGD attack with increasing  $\epsilon$  until the perturbed sample  $x_{\text{adv}} = x + \delta$  is differently classified or  $\epsilon$  reaches 1.0.
- 3) Once successful, the corresponding  $\epsilon$  and resulting adversarial sample are stored.

The hyperparameters used for PGD-based adversarial example generation are summarized in Table III.

### F. Constraint Adversarial Example Generation

We aim to induce adversarial examples through crosstalk by applying  $R_Y$  rotation gates on qubits adjacent to the target. On AQT hardware crosstalk is induced by single-qubit rotation gates.  $R_Z$  gates are implemented virtually on the AQT Ibex device, so adding extra  $R_Z$  rotations does not produce crosstalk. Consequently we restrict perturbations to the input components that are encoded in the  $R_Y$  gates.

TABLE III  
HYPERPARAMETERS USED FOR PGD-BASED ADVERSARIAL EXAMPLE GENERATION.

Hyperparameter	Value
Number of iterations $T$	100
Step size $\alpha$	0.01
Initial perturbation budget $\epsilon$	0.1
Perturbation budget increment	0.1
Maximum perturbation budget $\epsilon_{\text{max}}$	1.0
Norm constraint	$\ell_\infty$

1) *Implementation:* Let  $x^{(0)} \in \mathbb{R}^{16}$  denote the original input vector. We form the expanded input  $x \in \mathbb{R}^D$  used by the QNN by concatenating  $x^{(0)}$  three times,

$$x = (x_1^{(0)}, \dots, x_{16}^{(0)}, x_1^{(0)}, \dots, x_{16}^{(0)}, x_1^{(0)}, \dots, x_{16}^{(0)}) \in \mathbb{R}^{48},$$

that is  $D = 3 \cdot 16$ . The entries of this expanded vector are assigned to the encoding gates in the repeating order  $(R_Z, R_Y, R_Z)$ . In particular, the first triple consists of  $(x_1^{(0)}, x_2^{(0)}, x_3^{(0)})$ , not three copies of  $x_1^{(0)}$ .

We define a binary mask  $m \in \{0, 1\}^D$  that selects exactly the middle element of each  $(R_Z, R_Y, R_Z)$  triple,

$$m_k = \begin{cases} 1, & \text{if } k \in \{2, 5, 8, \dots, 47\} \\ 0, & \text{otherwise.} \end{cases}$$

This mask enforces that only components encoded in  $R_Y$  rotations may be perturbed. Given a differentiable loss  $\mathcal{L}(f(x), y)$  for model  $f$  and label  $y$ , a masked PGD step with step size  $\alpha > 0$  takes the form

$$g^{(t)} = m \odot \text{sign}(\nabla_x \mathcal{L}(f(x^{(t)}), y)), \quad \tilde{x}^{(t+1)} = x^{(t)} + \alpha g^{(t)},$$

followed by projection onto the  $\ell_\infty$  ball of radius  $\epsilon$  around the unperturbed expanded input  $x$ ,

$$x^{(t+1)} = \text{Proj}_{\|\cdot\|_\infty \leq \epsilon}[\tilde{x}^{(t+1)}].$$

We choose the same hyperparameters for the PGD procedure as in Section IV-E. For each evaluated training sample, success is declared if the predicted class label changes after the perturbation is applied. In this case, the current  $\epsilon$  is stored as the attack threshold for that sample.

2) *Determine which  $R_Y$  gates need to be applied:* Since our goal is to induce the intended effect in the QNN by exploiting crosstalk, we must determine which rotation gates to apply and where in the circuit to apply them in order to achieve the desired outcome. In what follows we derive these crosstalk factors exclusively from the AQT Ibex experiment described in Appendix B.

Specifically, we place the victim qubits on the ions  $[3, 5, 7, 9]$  and use the measurements of the five neighbor ions 2, 4, 6, 8, and 10 recorded in that experiment. For each measured qubit  $j \in \{2, 4, 6, 8, 10\}$  we estimate an effective  $R_Y$  angle from the observed bitstrings. Let  $p_1$  denote the proportion of outcomes equal to one at the bit position that corresponds to qubit  $j$ .

Consider a single qubit initially prepared in the state  $|0\rangle = (1 \ 0)^T$ . When a rotation about the  $Y$ -axis by an angle  $\theta_{\text{eff},j}$  is applied, the state transforms as  $R_Y(\theta_{\text{eff},j})|0\rangle = \begin{pmatrix} \cos(\frac{\theta_{\text{eff},j}}{2}) & \sin(\frac{\theta_{\text{eff},j}}{2}) \\ -\sin(\frac{\theta_{\text{eff},j}}{2}) & \cos(\frac{\theta_{\text{eff},j}}{2}) \end{pmatrix}^T$ .

The probability of obtaining the outcome  $|1\rangle$  when measuring in the computational basis is given by the squared magnitude of the lower amplitude:

$$p_1 = |\langle 1 | R_Y(\theta_{\text{eff},j}) | 0 \rangle|^2 = \sin^2\left(\frac{\theta_{\text{eff},j}}{2}\right).$$

Solving this expression for  $\theta_{\text{eff},j}$  yields

$$\sin\left(\frac{\theta_{\text{eff},j}}{2}\right) = \sqrt{p_1} \implies \theta_{\text{eff},j} = 2 \arcsin(\sqrt{p_1}).$$

For a given circuit with per gate angle  $\alpha$  applied  $r$  times in sequence we define the total applied angle

$$\theta_{\text{theo}} = r \alpha,$$

and the crosstalk factor on qubit  $j$

$$f_j = \frac{\theta_{\text{eff},j}}{\theta_{\text{theo}}}.$$

Qubits  $Q2$  and  $Q10$  each have a single adjacent qubit, namely  $Q3$  and  $Q9$  respectively, whereas  $Q4$ ,  $Q6$ , and  $Q8$  each have two adjacent qubits. Under a simple additive crosstalk model as a working assumption, the net induced rotation on a qubit scales approximately with the number of active neighbors. This explains why the central qubits exhibit larger factors than the edge qubits. If desired, one can normalize the theoretical angle by the number of adjacent attacker qubits, that is use  $\theta_{\text{theo}} = r \alpha$  for  $Q2$  and  $Q10$  and  $\theta_{\text{theo}} = 2r \alpha$  for  $Q4$ ,  $Q6$ , and  $Q8$ , which makes crosstalk factors more comparable. The smaller ion spacing toward the chain center qualitatively explains stronger crosstalk but is not included in our normalization. We keep  $r$  equal to 10 for  $Q2$  and  $Q10$ . The factor of two for  $Q4$ ,  $Q6$ , and  $Q8$  comes purely from the neighbor count normalization under the additive model.

The Table IV below reports these factors for the probe qubits  $Q2$ ,  $Q4$ ,  $Q6$ ,  $Q8$ , and  $Q10$  across all benchmarks.

TABLE IV  
CROSSTALK FACTORS  $f_j$  FOR QUBITS  $Q2$ ,  $Q4$ ,  $Q6$ ,  $Q8$ , AND  $Q10$  ACROSS BENCHMARK CIRCUITS.

Angle	Total angle	Q2	Q4	Q6	Q8	Q10
$\pi/100$	$\pi/10$	0.201	0.071	0.071	0.071	0.142
$\pi/8$	$10\pi/8$	0.016	0.013	0.011	0.013	0.016
$\pi/4$	$10\pi/4$	0.006	0.010	0.011	0.010	0.006
$3\pi/8$	$30\pi/8$	0.009	0.008	0.011	0.008	0.008
$\pi/2$	$10\pi/2$	0.007	0.010	0.010	0.010	0.007
$5\pi/8$	$50\pi/8$	0.008	0.009	0.011	0.011	0.009
$3\pi/4$	$30\pi/4$	0.007	0.009	0.011	0.011	0.007
$7\pi/8$	$70\pi/8$	0.006	0.010	0.011	0.011	0.007

The measurements indicate that  $f_j \approx 0.01$  in the majority of cases. Accordingly, for simplicity we set  $f_j = 0.01$  for all  $j$ .

Each of the 16 input dimensions is encoded in exactly one  $R_Y$  gate in the order

$$[2, 5, 8, 11, 14, 1, 4, 7, 10, 13, 16, 3, 6, 9, 12, 15].$$

The mapping from the 16 input dimensions to the  $R_Y$  gates is shown in Table V. The entries are the indices of the original input vector.

TABLE V  
ENCODING ORDER OF INPUT DIMENSIONS FOR THE  $R_Y$  GATES BY LAYER AND QUBIT.

Layer	Q3	Q5	Q7	Q9
1	2	5	8	11
2	14	1	4	7
3	10	13	16	3
4	6	9	12	15

See section IV-B for details on the re-upload encoding, architecture.

The masked PGD procedure described above yields an adversarial input vector  $x^{\text{adv}}$  whose nonzero perturbations are restricted to those components that are encoded via  $R_Y$  rotations. In order to realize this adversarial effect on quantum hardware through crosstalk, these abstract input-space perturbations must be translated into concrete physical operations applied to neighboring qubits. Each input dimension  $x_i$  is encoded into exactly one  $R_Y$  gate of the re-uploading circuit. Denoting by  $w_i$  and  $b_i$  the weight and bias parameters of the corresponding encoding gate, the effective rotation angle on the target qubit is given by

$$\theta_i = w_i x_i + b_i.$$

For an adversarial input  $x^{\text{adv}}$ , the desired change in the effective rotation angle is therefore

$$\Delta\theta_i = w_i (x_i^{\text{adv}} - x_i).$$

This quantity represents the angle offset that must be induced on the target  $R_Y$  gate in order to emulate the adversarial input at the circuit level.

We assume a linear crosstalk model in which a single-qubit  $R_Y$  rotation applied on a neighboring qubit induces a proportional, but attenuated, rotation on the target qubit. For a neighbor qubit  $j$ , this relation is modeled as

$$\theta_{\text{induced},j} = f_j \gamma_j,$$

where  $\gamma_j$  is the applied rotation angle on the neighbor and  $f_j$  is a hardware-specific crosstalk factor estimated experimentally.

For a target qubit with two adjacent neighbors, the total induced rotation is assumed to be additive,

$$\theta_{\text{induced}} = f_{\text{left}} \gamma_{\text{left}} + f_{\text{right}} \gamma_{\text{right}}.$$

To avoid overfitting to device-specific variations, we adopt a uniform crosstalk factor  $f_j = f$  for all neighbors. Under this assumption, applying identical rotations  $\gamma$  on both adjacent qubits yields

$$\theta_{\text{induced}} = 2f \gamma.$$

To induce a desired target offset  $\Delta\theta_i$ , the required neighbor rotation angle is therefore

$$\gamma = \frac{\Delta\theta_i}{2f}.$$

These rotations are applied symmetrically to all qubits adjacent to the target qubit hosting the corresponding  $R_Y$  gate.

a) *Amplitude saturation and gate splitting*: Due to the native pulse implementation on the AQT hardware, requested  $R_Y$  rotations with magnitude larger than  $\pi$  do not yield stronger physical pulses. Instead, they are decomposed into equivalent equatorial rotations sandwiched by virtual  $R_Z$  gates, which do not contribute to crosstalk. Consequently, neighbor rotations are saturated at magnitude  $\pi$ ,

$$\gamma_{\text{applied}} = \text{sign}(\gamma) \min(|\gamma|, \pi).$$

If  $|\gamma| > \pi$ , the required disturbance is implemented as a sequence of multiple  $R_Y(\pm\pi)$  rotations followed by a final residual rotation, ensuring that the cumulative induced effect approximates the desired  $\Delta\theta_i$ .

## V. RESULTS

In line with the methodological structure introduced in Section IV, we present and discuss the results according to the same multi-stage attack pipeline.

### A. Stage 1: Side-Channel Reconnaissance

Before generating the power trace, the victim QNN circuit is transpiled into the native AQT gates with `optimization_level=0` to ensure that every gate is preserved exactly as written, without any simplification or merging. Once the circuit is in this basis, we execute the power trace simulator to generate  $\{(t_k, P_k)\}_{k=0}^K$ .

1) *Experimental Results*: We begin by fixing a single training sample and computing its corresponding victim QNN power trace

$$(\{t_k^{(v)}\}, \{P_k^{(v)}\}).$$

Next, for each benchmark circuit  $j \in \{1, 2, \dots, 24\}$ , we computed the corresponding power trace  $(\{t_k^{(j)}\}, \{P_k^{(j)}\})$ . We then compare these traces in three steps:

a) *1. Timing Filter*: We first eliminate any benchmarks whose total execution duration differs from the victim's trace. Concretely, we compute

$$T^{(j)} = \max(t_k^{(j)}), \quad T^{(v)} = \max(t_k^{(v)}),$$

and retain only those  $j$  for which  $T^{(j)} = T^{(v)}$ . In our case, this reduces the original 24 candidates to just three, namely the benchmark circuits composed of four layers acting on four qubits.

b) *2. Distance Metric*: Let

$$\Delta_{\text{step}} = 1 \mu\text{s}.$$

For each original interval  $[t_{k-1}, t_k)$  with  $k = 1, \dots, K$ , define

$$M_k = \frac{t_k - t_{k-1}}{\Delta_{\text{step}}} \in \mathbb{N},$$

and introduce the intermediate times

$$\tilde{t}_{k,m} = t_{k-1} + m \Delta_{\text{step}}, \quad m = 0, 1, 2, \dots, M_k - 1,$$

so that  $\tilde{t}_{k,m} < t_k$  for all  $m$ . For the case  $k = K$ , we append a single final point at the very end of the trace:

$$\tilde{t}_{K,M_K} = t_K, \quad \text{and assign } \tilde{P}_{K,M_K} = P_K.$$

Thus, the total number of fine-grid points is

$$N = \sum_{k=1}^K M_k + 1,$$

where the “+1” accounts for the endpoint  $(t_K, P_K)$ .

We enumerate all points on the fine grid  $\{\tilde{t}_n\}_{n=0}^N$  in lexicographic order on the pairs  $(k, m)$ . With this definition, the forward-filled amplitude at each  $\tilde{t}_n$  is simply

$$\tilde{P}_n = P_k \quad \text{whenever } \tilde{t}_n \in [t_{k-1}, t_k), \quad \tilde{P}_N = P_K.$$

Denote the resulting discrete sequences by  $\{P_n^{(v)}\}_{n=0}^N$  and  $\{P_n^{(j)}\}_{n=0}^N$ . We then compute for each candidate  $j$  the Euclidean distance

$$d_j = \sqrt{\sum_{n=0}^N (P_n^{(j)} - P_n^{(v)})^2}, \quad (1)$$

which quantifies the total  $L^2$ -deviation between the two power profiles on the same microsecond-resolution grid.

c) *3. Best Match*: Sorting the distances  $\{d_j\}$  in ascending order yields

$$\begin{aligned} d_7 &\approx 9.84, \\ d_9 &\approx 119.14, \\ d_8 &\approx 132.14. \end{aligned}$$

Thus, benchmark circuit 7 has the smallest distance and is selected as the best match, confirming that it indeed corresponds to the victim QNN's structure. Note that the concrete distance values depend on the specific  $R_Y$  rotation parameters and on the concrete training sample encoded in the QNN. In our evaluated instances, circuit 7 consistently yields the smallest  $L^2$ -deviation among benchmark circuits 7, 8, and 9, indicating that it is the best structural match to the victim QNN. Since the attacker can infer the concrete structure of the victim QNN, they can now leverage this information to place targeted disturbance gates on neighboring qubits at specific points in time during the execution of the victim QNN. The concrete simulated power traces corresponding to the  $L^2$ -deviation displayed in V-A1c are shown in Appendix C.

### B. Stage 2: Adversarial Examples

As discussed in Section IV-E we use the PGD algorithm to generate adversarial examples for the 1000 training samples. To visualize the effect of such adversarial perturbations in the original image space, we performed an inverse PCA transformation of the adversarial examples back into the  $16 \times 16$  pixel domain. This enables a visual comparison between the true image and its adversarially perturbed counterpart. We repeat this reconstruction for several samples at different perturbation magnitudes  $\epsilon$ . For each case, Figure 4 shows a side-by-side visualization of the original image and its corresponding adversarial variant in the pixel domain.

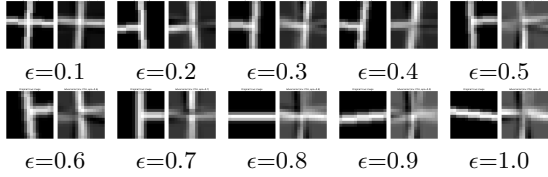


Fig. 4. Overview of side-by-side visualizations of original (left) and adversarial (right) samples for various attack strengths  $\epsilon$ . Each panel shows the reconstructed pair from PCA space to the  $16 \times 16$  pixel domain for a selected training sample.

The following Table VI presents the distribution of the minimum  $\epsilon$  values required to generate successful adversarial examples for the training set using PGD, as described above. For each sample, the smallest  $\epsilon \leq 1.0$  that sufficed to trigger misclassification is recorded. The column **Original correct** indicates how many of these adversarial examples were generated from samples that the QNN originally classified correctly and were subsequently misclassified after adversarial perturbation. The column **Label flipping** counts cases where the original prediction was incorrect, but the adversarial example caused the prediction to switch to the correct class. Notably, for 160 out of 1000 training samples, no adversarial perturbation with  $\epsilon \leq 1.0$  could be found.

TABLE VI  
HISTOGRAM OF MINIMUM  $\epsilon$  REQUIRED FOR PGD TO GENERATE ADVERSARIAL EXAMPLES ON THE TRAINING SET.

$\epsilon$	#Samples	Correct	Flipped
0.1	63	54	5
0.2	87	81	3
0.3	92	90	0
0.4	81	77	1
0.5	87	83	0
0.6	104	103	0
0.7	88	87	0
0.8	83	79	0
0.9	71	59	0
1.0	84	78	0
<b>No adversarial example (<math>\epsilon &gt; 1.0</math>):</b>			<b>160</b>

As shown in Table VI, PGD produced successful adversarial examples with  $\epsilon \leq 1.0$  for 840 out of 1000 training samples. When evaluating the QNN on the resulting adversarially

perturbed inputs, the classification accuracy decreased from 92.4% on the original inputs to 1.07% under adversarial perturbations.

### C. Stage 3: Adversarial Generation on Surrogates

In contrast to the first approach, we only consider those samples from the training data that are correctly classified by the QNN when evaluated on the PennyLane statevector simulator. Hence, we considered 885 out of 1000 samples for the surrogate-based adversarial example generation. The following Table VII presents the distribution of the minimum  $\epsilon$  values required to generate successful adversarial examples for the training set using masked PGD, as described in Section IV-F.

TABLE VII  
HISTOGRAM OF MINIMUM  $\epsilon$  VALUES NEEDED FOR MASKED PGD TO GENERATE ADVERSARIAL EXAMPLES ON THE TRAINING SET.

Epsilon value	Number of samples
0.1	33
0.2	28
0.3	31
0.4	50
0.5	40
0.6	28
0.7	35
0.8	28
0.9	33
1.0	32
<b>No adversarial example (<math>\epsilon &gt; 1.0</math>):</b>	
	<b>547</b>

As expected, it is quite hard to find adversarial examples given the relatively strong constraint that only inputs encoded in  $R_Y$  gates can be manipulated. We evaluate three variants per selected training sample namely **clean** with the original input, **adversarial** with an adversarially perturbed input and **crosstalk** that approximates the adversarial sample through neighbor  $R_Y$  rotations on adjacent qubits. Conceptually  $x_{\text{crosstalk}}$  is an approximation to  $x_{\text{adv}}$  with effective angles induced via rotations on the neighbors. From the 338 training samples for which a successful adversarial example was constructed on the PennyLane surrogate, we randomly select 50 for execution on the AQT Ibex hardware. The QNN qubits are placed at the given physical positions [3, 5, 7, 9] and neighbor  $R_Y$  rotations are applied according to the left and right neighbors of each target qubit. All  $150 = 3 * 50$  circuits are transpiled with `optimization_level = 0`. This layout implies that some disturbance qubits are shared between two QNN qubits. For instance, a rotation applied to Q4 can induce crosstalk on both Q3 and Q5. This experiment is specific to the trapped-ion setting considered here. On AQT Ibex, the qubits form a linear ion chain and single-qubit rotations are applied by addressing individual ions, where residual illumination of neighbouring ions can induce measurable crosstalk. Moreover, gates are executed sequentially on this device, which makes it meaningful to place disturbance rotations at specific points in the victim circuit.

We compute the  $Z$  expectation values for the measured QNN qubits and assign the predicted class label as the argmax over the four expectation values. Accuracy is the fraction of correct predictions over the 50 samples as summarized in Table VIII.

TABLE VIII  
QNN ACCURACY ON 50 RANDOMLY SELECTED ADVERSARIALLY SUSCEPTIBLE TRAINING SAMPLES.

Image	Accuracy
clean image	0.64
adversarial image	0.56
crosstalk image	0.68

These results are counterintuitive because the accuracy on the clean images is lower than expected and the overall differences, in terms of accuracy, between the three classes are smaller than anticipated. This can be explained by the fact that the selected samples were chosen based on their behaviour under the PennyLane statevector simulator, whereas the reported accuracies are obtained from AQT Ibex hardware. Consequently, samples that are correctly classified by the simulator need not remain correctly classified under hardware and shot noise. To quantify how well the AQT Ibex hardware results approximate the PennyLane statevector simulator we compare the four dimensional expectation value vectors for each sample. Let  $e_i^{(A)} \in \mathbb{R}^4$  and  $e_i^{(B)} \in \mathbb{R}^4$  denote the expectation values of two sources  $A$  and  $B$  for sample  $i$ , for example,  $A$  refers to the PennyLane statevector simulator and  $B$  to the AQT Ibex hardware.

The mean absolute error (MAE) for this sample  $i$  is defined as

$$\Delta := \text{MAE}_i(A, B) = \frac{1}{4} \sum_{k=1}^4 |e_{i,k}^{(A)} - e_{i,k}^{(B)}|. \quad (2)$$

Averaging over all  $N = 50$  samples yields

$$\overline{\text{MAE}}(A, B) = \frac{1}{N} \sum_{i=1}^N \text{MAE}_i(A, B). \quad (3)$$

To illustrate the spread of deviations across the inputs we inspect samples with particularly large and particularly small MAE between hardware and PennyLane statevector simulator expectation values. Figure 5 shows the two unperturbed samples with the largest observed deviations and the two unperturbed samples with the smallest deviations. In each panel we plot the four expectation values from hardware and from the simulator.

We evaluate the mean absolute error between the full four-dimensional expectation value vectors for all source pairs. Here, `hw_clean` denotes the AQT Ibex hardware expectation values for the original clean inputs, `hw_adv` the hardware expectation values for the adversarially perturbed inputs obtained by masked PGD, and `hw_crosstalk` the hardware expectation values for the clean inputs executed with additional neighbour  $R_Y$  rotations designed to induce an adversarial crosstalk pattern. Analogously, `model_clean`

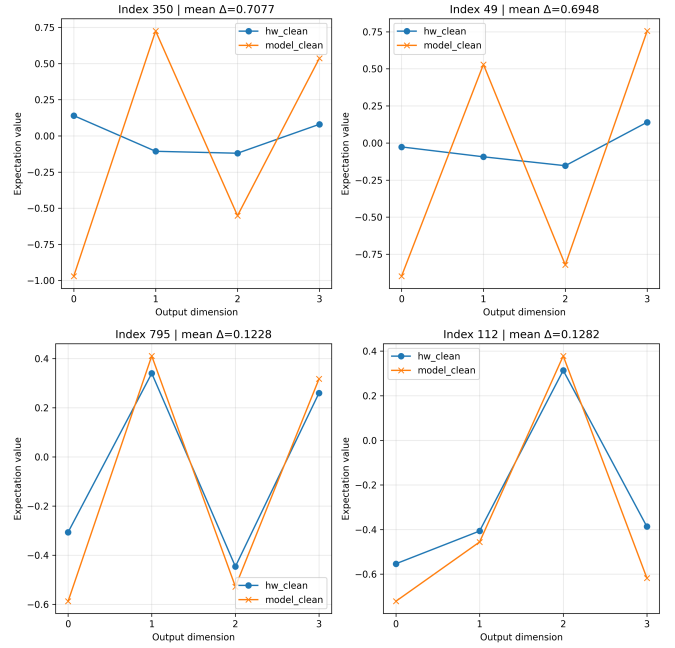


Fig. 5. Above Two samples with the largest mean absolute error. Below Two samples with the smallest mean absolute error.

and `model_adv` denote the PennyLane statevector simulator expectation values for the clean and adversarial inputs, respectively.

Using the definition of the average mean absolute error in eq. (3), Table IX reports  $\overline{\text{MAE}}(A, B)$  for all pairs  $(A, B)$ , averaged over all fifty samples. In the extended report [7], we also consider confidence-based sample selection, focusing on inputs for which the victim QNN exhibits either the highest or the lowest predictive certainty when evaluated using the PennyLane statevector simulator.

TABLE IX  
MEAN ABSOLUTE ERROR BETWEEN EXPECTATION VALUE VECTORS FOR ALL PAIRS OF HARDWARE AND SIMULATOR SOURCES, AVERAGED OVER FIFTY SAMPLES.

Pair	$\overline{\text{MAE}}$
hw_adv vs hw_crosstalk	0.1236
hw_clean vs hw_crosstalk	0.1270
hw_clean vs hw_adv	0.1452
model_clean vs model_adv	0.1682
hw_adv vs model_adv	0.2532
hw_clean vs model_adv	0.2745
hw_crosstalk vs model_adv	0.2831
hw_clean vs model_clean	0.3086
hw_crosstalk vs model_clean	0.3294
hw_adv vs model_clean	0.3534

It is encouraging that the smallest mean absolute error is observed for the pair `hw_adv` versus `hw_crosstalk`.

This indicates that the crosstalk construction indeed moves the hardware evaluation of the clean inputs closer to the adversarial hardware behavior, which is precisely the intended purpose of the `hw_crosstalk` configuration.

## VI. DISCUSSION

### A. Key Findings

In this paper, we executed a multi-stage attack on AQT trapped-ion hardware. During the reconnaissance stage, the power-trace attack enabled the most direct and reliable reconstruction of the victim QNN architecture. Without any circuit-level optimization, the comparison with benchmark circuits yielded an unambiguous result, allowing us to infer the complete QNN architecture. A broader comparison with crosstalk-based and timing-based reconnaissance attacks is provided in the QML-ESA report [7], where power traces emerge as the strongest among the evaluated approaches. The report further demonstrates that the weights and bias parameters encoded in the  $R_Y$  gates can be reverse engineered. This, however, is generally not possible for parameters encoded in  $R_Z$  gates, as these gates are implemented virtually. Furthermore, the adversarial-example results in Section V-B show that the trained QNN is highly vulnerable to input-space perturbations: PGD succeeds on a large majority of the analyzed training samples and causes a near-complete collapse in classification accuracy under adversarial perturbation.

In addition, in the report [7], we analyze transfer attacks and show that adversarial examples constructed under statevector simulation partially retain their effectiveness when executed on real superconducting and trapped-ion hardware. While backend noise reduces the overall misclassification rates, the decision-boundary shifts induced by the adversarial perturbations persist across different hardware platforms.

The approximation of Adversarial examples via Crosstalk proved successful in the sense that the  $\overline{\text{MAE}}$  is minimized between the adversarial examples and the original samples perturbed through crosstalk, as outlined in Table IX. A potential extension of the crosstalk-based adversarial example construction concerns the choice of qubit layout. In the current experiments, the victim QNN qubits reside on the physical qubits [3, 5, 7, 9], which implies that inducing a disturbance on one target qubit necessarily requires applying rotation gates to its physical neighbours. For example, attempting to perturb qubit Q3 via its neighbours Q2 and Q4 inevitably affects qubit Q5 as well, since the applied  $R_Y$  rotations on Q4 induce crosstalk on both adjacent qubits. It would therefore be interesting to explore whether alternative, intentionally non-standard layouts, such as placing the QNN qubits on positions [2, 5, 8, 11], could strengthen the attack. In such a configuration, the disturbance qubits [1, 4, 7, 10] would interface with the QNN without unintentionally influencing additional neighbours. However, it must be emphasised that such layouts are not typical and should be regarded primarily as an academic construct aimed at probing the limits of crosstalk-induced adversarial manipulation.

### B. Defensive Strategies

1) *Power Traces*: To mitigate the risk of power side-channel attacks several defensive strategies have been proposed in the literature. According to [6], the following approaches represent the most immediate and effective lines of defense:

- **Decoy Pulses**: Executing calculation-independent gates that do not contribute to the original circuit but interfere with the power trace profile, which makes circuit reconstruction computationally more expensive (increasing number of variables) and noisier (more influence of parallel gates)
- **Power Randomization**: Introducing random variations in power consumption, such as randomized pulse timing, or stochastic load activation
- **Constant-Power Operation**: Designing the arbitrary waveform generators (AWGs) or FPGA-based controllers to maintain a constant power profile regardless of whether quantum pulses are being generated or idle

These countermeasures, inspired by classical side-channel defenses, require adaptation to the control architectures of quantum computers [6].

2) *Adversarial Examples*: A fundamental prerequisite for robustness in machine learning systems is a thorough understanding of the model’s behavior under adversarial conditions and the integration of corresponding defense mechanisms during training. Quantum neural networks, similar to their classical counterparts, can benefit from two key strategies: adversarial training and regularization. Adversarial training involves deliberately exposing the model to perturbed inputs during training, thereby enabling it to generalize better under adversarial stress. This method is conceptually simple and has proven effective in increasing robustness in both quantum and classical domains. More rigorous claims of robustness can be made when restricting the Lipschitz bound of the model’s encoding Hamiltonians, via Lipschitz regularization of the quantum model. Lipschitz bounds quantify how much a model’s output can change concerning small changes in its input. Lower Lipschitz bounds signify that a model is less sensitive to such changes, making it inherently more robust against adversarial attacks [2, 22].

3) *Adversarial Examples via Crosstalk*: The adversarial examples discussed in Section V-C, although restricted to perturbations on input components encoded in  $R_Y$  rotations, constitute genuine adversarial manipulations of the QNN. For this reason, the defensive mechanisms discussed for adversarial examples, apply equally in the present context. Both approaches reduce the model’s sensitivity to local input variations and thus mitigate the effectiveness of adversarial examples. In addition to model-level defenses, effective protection against crosstalk-based adversarial behavior also requires system-level measures. The most direct and robust defence is to avoid situations in which multiple users share the same quantum processor at the same time.

If no shared-execution scenario is permitted, an adversary cannot place rotation gates on neighboring qubits and therefore cannot induce effective angles on the victim circuit. Preventing shared execution removes this attack vector entirely. A further defensive consideration arises from the fact that an attacker must possess sufficiently accurate knowledge of the execution time of the victim circuit in order to place disturbance gates at the correct positions in time. For this reason, defensive mechanisms against model-stealing attacks are relevant.

### C. Ethics

All experiments presented in this paper were conducted in controlled research settings and exclusively on quantum hardware and simulators to which the authors had legitimate access. No production systems, customer workloads, or confidential user data were targeted or affected. The primary motivation of this work is to contribute to the secure design and deployment of quantum computing and QML systems. By systematically exposing attack vectors and their interdependencies, the results aim to inform hardware providers, cloud operators, and QML practitioners about potential risks that may not be apparent from isolated threat analyses.

## VII. CONCLUSION

In this work, we presented an end-to-end, multi-stage kill-chain attack against a QNN executed on real trapped-ion quantum hardware. By chaining side-channel reconnaissance, adversarial example generation, and hardware-induced crosstalk manipulation, we demonstrated that vulnerabilities across different abstraction layers of quantum machine learning systems can be combined into a coherent attack pipeline. Our results show that information leaked through side channels, in particular power traces, enables the inference of the victim QNN’s architectural structure, which in turn allows the attacker to construct targeted noise-injection attacks. Overall, these findings highlight the necessity of analyzing QML security from a system-level perspective, rather than treating noise, crosstalk, and adversarial robustness as independent phenomena.

### ACKNOWLEDGMENT

This research is part of the *QML-ESA* (Extended Security Analysis of Quantum Machine Learning) project, which is funded by the German Federal Office for Information Security (BSI) [7].

## APPENDIX A SUPERCONDUCTING EXPERIMENTS

### A. Stage-by-Stage Outcomes

As in the trapped-ion case, we explored side-channel attacks based on crosstalk, timing, and power traces. Since the power-trace attack is the most promising among these, it is discussed in the appendix. With respect to noise injection, we briefly address the Active SWAP attack in the appendix, while a substantially more detailed treatment of this attack, alongside other attack vectors, is provided in the extended report [7].

1) *Power Trace Attack*: As in the trapped-ion case, we do not have access to actual power traces, we base all experiments on power traces computed from pulse schedules. More specifically, we generate pulse schedules and power traces from IBM’s simulated pulse backend *Fake7QPulseV1*<sup>3</sup>, which provides an interface to the pulse-level information for each qubit in the circuit. The target circuit and its transpiled version is shown in Figure 6. This toy circuit consists of two qubits and five gates: Two single-qubit gates on each qubit, namely a  $\sqrt{X}$  gate followed by an  $X$  gate and their permuted version, and one CNOT between the first and the second qubit. During transpilation, this circuit is decomposed into an  $R_Z - \sqrt{X} - R_Z$  gate combination on both the first and the second qubit, followed by the CNOT gate. Notably,  $R_Z$  gates are implemented as *virtual gates* on the IBM superconducting hardware, which leaves no measurable effect on the power trace.

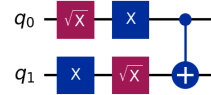


Fig. 6. Toy-CX test circuit: original (top) and after transpilation (bottom).



For the first experiment, we use the pulse simulator to generate noise-free per-channel power traces. Given the toy circuit as described, the resulting power trace schedule is depicted in Figure 7.

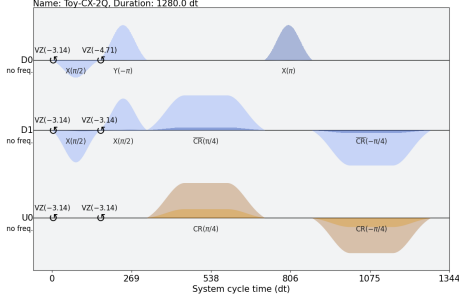
As described in the report [7], the objective of an attacker can be stated as

$$A_{PL} = \arg \min_{A'_{PL}} \sum_{c \in C} d \left\{ \text{Power}_c[A'_{PL}](x), v_c(x) \right\},$$

where a simple per-channel analysis of the power trace signatures of the target and benchmark circuits is enough to determine the most likely candidate. Some details of the template scoring are shown in Table X. For each relevant time

<sup>3</sup>[https://docs.quantum.ibm.com/api/qiskit/1.0/qiskit.providers.fake\\_provider.Fake7QPulseV1](https://docs.quantum.ibm.com/api/qiskit/1.0/qiskit.providers.fake_provider.Fake7QPulseV1)

Fig. 7. Pulse Schedule for Toy-CX Test Circuit



step the lowest score is chosen and while the resulting channel occupation constraints are tracked. This results in some per-time-step ranking lists being shorter than others as in the case of  $t = 0$  for the *second* qubit.

TABLE X  
JENSEN-SHANNON DISTANCE SCORING AND RANKING OF GATE TEMPLATES AT KEY TIMES STEPS (0, 160)

Rank	$t$	Gate	Qubit	$\sqrt{\text{JSD}}$
1	0	SX	0	<b>0.0000000</b>
2	0	SX	1	0.00000000
3	0	X	0	0.00000582
4	0	X	1	0.00027877
5	0	CX	0,1	1.84281222
6	0	CX	1,0	1.89385275
1	0	SX	1	<b>0.0000000</b>
2	0	X	1	0.00027877
1	160	CX	0,1	<b>0.0000000</b>
2	160	SX	1	0.00000000
3	160	X	0	0.00000000
4	160	SX	0	0.00000582
5	160	X	1	0.00027877

From this table the schedule can be easily reconstructed as shown in Table XI. As noted, the reconstruction results only include SX gates since we cannot measure the effect of virtual  $R_Z$  gates in the power trace.

TABLE XI  
RECONSTRUCTED GATE SCHEDULE FOR TOY-CX CIRCUIT USING A PER-CHANNEL POWER TRACES.

$t_s$	gate	qubit
0	SX	0
0	SX	1
160	CX	0,1

The situation changes when the information leakage is restricted to the combined power trace, where the sum of individual gates makes it hard for an attacker to infer which gates were executed at which timestep on which qubit. This issue becomes clear when looking at Figure 7 and Figure 8 as we can directly infer which gate is executed on which qubit in the per-channel power trace schedule; however, for the summed total power trace, this is not trivially possible as

permuted gate-to-qubit assignments may lead to similar total power traces.

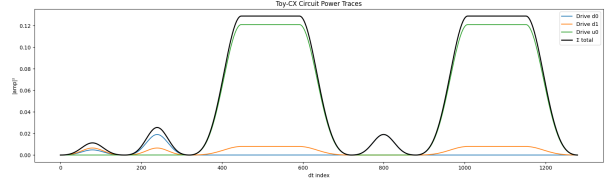


Fig. 8. Per-Channel and Total Power Trace for Toy-CX Test Circuit

In the QML-ESA report [7], we discuss how to tackle this challenge.

2) *Active SWAP Attack*: In the Active SWAP attack, to our knowledge first introduced by [12], the attacker executes a single CNOT gate concurrently with the victim’s circuit on a cloud-based, multi-tenant quantum system in order to induce errors in the victim’s output. The purpose of this attack is to disturb the computation of the victim QNN and thereby reduce the accuracy of the model. Based on the QNN layout identified by the attacker during the reconnaissance phase, a benchmark circuit is constructed by applying a Hadamard gate to each QNN qubit. For each candidate pair of qubits, the attacker executes a fixed number of shots while concurrently applying a single CNOT gate together with this benchmark circuit. The resulting bitstring distribution is then compared to the uniform distribution, which is the expected outcome of the benchmark circuit in the absence of the disturbing CNOT gate, using the trace distance between the two probability distributions. The trace distance is defined as

$$D(P, Q) \equiv D(p_x, q_x) = \frac{1}{2} \sum_x |p_x - q_x|, \quad (4)$$

where  $P = \{p_x\}_x$  and  $Q = \{q_x\}_x$  are two probability distributions over the same index set. Qubit pairs that maximize this trace distance are selected, as they are expected to induce the strongest crosstalk effects and are therefore used to interfere with the execution of the victim QNN. As discussed in depth in the report [7], it is appropriate to consider a benchmark circuit that does not require any SWAP operations in order to be executed on the device.

The experiment is performed on the 54-qubit IQM Emerald superconducting device. The physical qubit layout used for this experiment is shown in Figure 9. The victim QNN is placed on the physical qubits [18, 19, 26, 27], while candidate disturbance CNOTs are swept across the remaining device.

We fix qubit 1 and sweep the second qubit  $j$  across the device. For each candidate index  $j$ , we construct a quantum circuit by applying a CNOT from qubit 1 to qubit  $j$ . Now we apply a Hadamard gate on each of the qubits [18, 19, 26, 27] and measure those four target qubits. We record the resulting bitstring distribution and compute its trace distance to the uniform distribution. We rank the CNOT pairs by their trace distance to the uniform distribution and summarize the top five in Table XII.

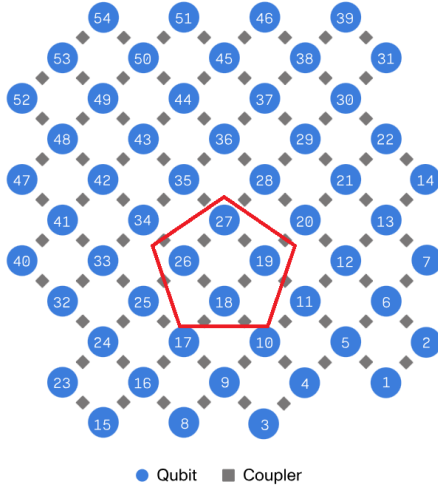


Fig. 9. Physical qubit layout of the 54-qubit IQM Emerald device. The red outline indicates the qubits used for the victim QNN in the Active SWAP experiment.

TABLE XII

TOP FIVE CNOT PAIRS BY TRACE DISTANCE (CONTROL QUBIT 1).

CNOT Pair	Trace Distance
(1, 42)	0.1018
(1, 43)	0.0859
(1, 34)	0.0857
(1, 38)	0.0825
(1, 36)	0.0806

In a second run, we fix qubit 54 and sweep the second qubit  $j$  across the device. For each candidate index  $j$ , we construct a quantum circuit by applying a CNOT from qubit 54 to qubit  $j$ , apply the Hadamard gates on physical qubits [18, 19, 26, 27] and then measure those four target qubits. We rank the CNOT pairs by their trace distance to the uniform distribution and summarize the top five in Table XIII.

TABLE XIII

TOP FIVE CNOT PAIRS BY TRACE DISTANCE (CONTROL QUBIT 54).

CNOT Pair	Trace Distance
(54, 3)	0.1472
(54, 4)	0.1084
(54, 9)	0.0918
(54, 15)	0.0708
(54, 10)	0.0706

In the following plot 10 we compare the bitstring distributions of the candidate CNOT pairs [(1, 42), (54, 3)] with the uniform distribution.

Those plots suggest that applying a CNOT on one of those pairs induces a significant amount of noise in the victim QNN, since they induce a significantly different bitstring distribution compared to the expected uniform distribution

When we calculate the accuracy of the QNN on 100 test images with 25 images per class, we get the following XIV:

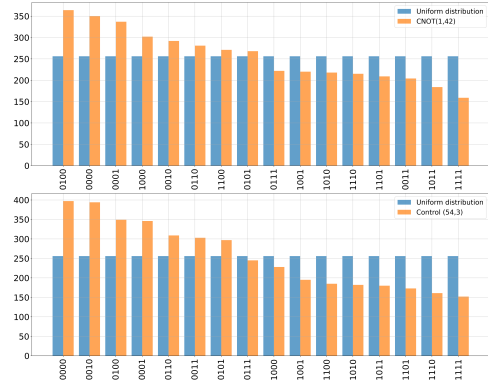


Fig. 10. Bitstring distribution comparison between the uniform distribution and disturbance. *left* disturbance on (1, 42) *right* disturbance on (54, 3)

TABLE XIV

QNN ACCURACY ON 100 TEST IMAGES FOR EACH DISTURBANCE.

CNOT Pairs	Accuracy
no disturbance	0.8
(1, 42)	0.87
(54, 3)	0.88
(1, 42), (54, 3)	0.75

It is interesting to note that applying either CNOT(1, 42) or CNOT(54, 3) individually leads to an increase in the model’s accuracy compared to the undisturbed case. However, when both CNOTs are applied simultaneously, the accuracy of the model actually decreases. This should not be interpreted as a systematic accuracy improvement caused by the disturbance CNOTs. Rather, the disturbances can have a counterintuitive stabilising effect on this particular set of test images by reducing specific misclassification patterns. At the same time, the combined disturbance changes the misclassification behaviour more strongly and shifts errors from one class to another, which is consistent with the observed decrease in overall accuracy.

A clear view of the classification behaviour under each disturbance scenario is obtained by examining the corresponding confusion matrices. Figure 11 compares the confusion matrices for the baseline execution, the two individual disturbances (1, 42) and (54, 3), and the combined disturbance.

In the report [7], we further discuss a topology-aware Active SWAP attack, where the idea is to take advantage of the topology of the quantum hardware to find more suitable CNOT gate candidates for influencing the victim circuit.

## APPENDIX B

### AQT CROSSTALK EXPERIMENT

We aim to explore the concept of crosstalk signature analysis on the AQT Ibex 12-qubit device. As discussed in Section III-D, on trapped-ion devices, crosstalk is primarily induced by single-qubit rotations. We began with a proof-of-concept attack, in which the victim circuit consists of four qubits located on ions 3, 5, 7, and 9. On each qubit, we apply ten  $R_Y$  gates with an angle of  $\pi/2$ , inserting a barrier after each gate

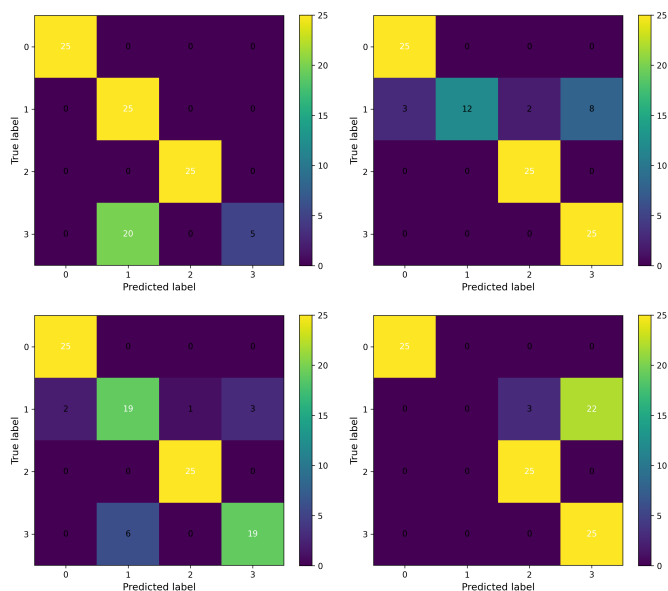


Fig. 11. Confusion matrices for the baseline execution (top left), disturbances on qubit pairs (1, 42) (top right) and (54, 3) (bottom left), and the combined disturbance on (1, 42) and (54, 3) (bottom right).

to prevent the compiler from combining them into a single  $R_Y$  rotation. We want to collect a crosstalk signature by measuring the neighboring ions [2, 4, 6, 8, 10].

In the following Figure 12, the victim circuit is illustrated:

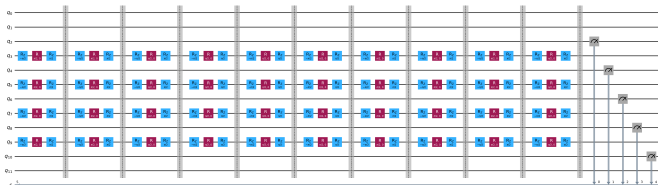


Fig. 12. A conceptual overview of the victim circuit.

We performed the maximum of 2000 shots per job and obtained the bitstring distribution shown in Table XV.

TABLE XV  
MEASURED BITSTRING DISTRIBUTION OVER 2000 SHOTS ON THE AQT IBEX DEVICE.

Bitstring	Counts
00000	1849
00010	44
00100	51
01000	42
00001	6
10000	6
01100	1
00110	1

The table clearly shows that crosstalk is induced on the neighboring ions of the AQT Ibex device. In a noise-free scenario, we would expect to observe the bitstring 00000 in all 2000 shots. However, it is notable that qubits 4, 6, and 8 are

measured in the 1 state significantly more often than the edge qubits 2 and 10. This observation can be explained by the fact that qubits 4, 6, and 8 each have two neighboring qubits on which the  $R_Y$  gates are applied, making them more susceptible to crosstalk effects compared to the edge qubits, which only have one such neighbor. In addition, these (physical) ions are positioned more centrally, where the spacing between ions is smaller than at the ends of the chain. Consequently, the induced crosstalk is higher in the center than at the edges, further increasing the likelihood of measuring 1 on ions 4, 6, and 8.

To investigate how the crosstalk signature depends on the rotation angle, we conducted a set of benchmark circuits. In each benchmark circuit, we applied ten consecutive  $R_Y(\theta)$  gates on the same four qubits, with  $\theta$  taking values from the set  $\{\pi/100, \pi/8, 2\pi/8, 3\pi/8, 4\pi/8, 5\pi/8, 6\pi/8, 7\pi/8, 8\pi/8\}$ . After each gate, a barrier is inserted to prevent circuit optimization by the compiler. For every angle, we perform 2000 shots and measure the five neighboring ions [2, 4, 6, 8, 10] to characterize the pattern of crosstalk as a function of the applied rotation.

We calculate the qubit-based mean squared error

$$\text{MSE}(s_x^{(\text{victim})}, s_j^{(\text{bench})}) = \frac{1}{n} \sum_{i=1}^n (y_i^{(\text{victim})} - y_{ij}^{(\text{bench})})^2, \quad (5)$$

where

- $n = 5$  is the number of “listening” qubits,
- $y_i^{(\text{victim})}$  is the measured frequency of outcome 1 on the  $i$ -th listening qubit for the victim circuit
- $y_{ij}^{(\text{bench})}$  is the corresponding frequency for the  $i$ -th qubit in benchmark circuit  $j$ .

to compare the crosstalk signatures of the benchmark circuits with that of the victim circuit. The results are shown in the following Table XVI.

TABLE XVI  
BENCHMARK CIRCUITS SORTED BY QUBIT-BASED MSE.

Rotation Angle	(qubit-based) MSE
$4\pi/8$	0.0000047
$3\pi/8$	0.0000895
$2\pi/8$	0.0001704
$5\pi/8$	0.0002433
$\pi/8$	0.0002739
$\pi/100$	0.0003223
$8\pi/8$	0.0003227
$6\pi/8$	0.0007585
$7\pi/8$	0.0022040

This result is very encouraging, as the lowest mean squared error is achieved for the benchmark circuit with rotation angle  $4\pi/8 = \pi/2$ , which exactly matches the angle used in the victim circuit. This shows that the attack succeeded in inferring the rotation angle solely on the basis of observed crosstalk signature. When comparing the number of observed 00000 bitstrings in the victim circuit with the benchmark circuits, it becomes apparent from Table XVII that the benchmark circuit

with rotation angle  $4\pi/8 = \pi/2$  yields a count closest to the victim. This is exactly the rotation angle that was applied in the victim circuit.

TABLE XVII  
NUMBER OF OCCURRENCES OF BITSTRING 00000 FOR EACH ROTATION ANGLE.

Rotation Angle	Counts of 00000
$\pi/100$	1998
$\pi/8$	1986
$2\pi/8$	1957
$3\pi/8$	1935
$4\pi/8$	1839
$5\pi/8$	1731
$6\pi/8$	1660
$7\pi/8$	1516
$8\pi/8$	1489

The results show that the crosstalk increases with the rotation angle. Larger rotation angles induce stronger crosstalk and thus fewer 00000 counts.

APPENDIX C  
SIMULATED AQT POWER TRACES

The following plots show the simulated power traces of benchmark circuits 7, 8, and 9 discussed in Section V-A, each compared against the power trace of the victim QNN.

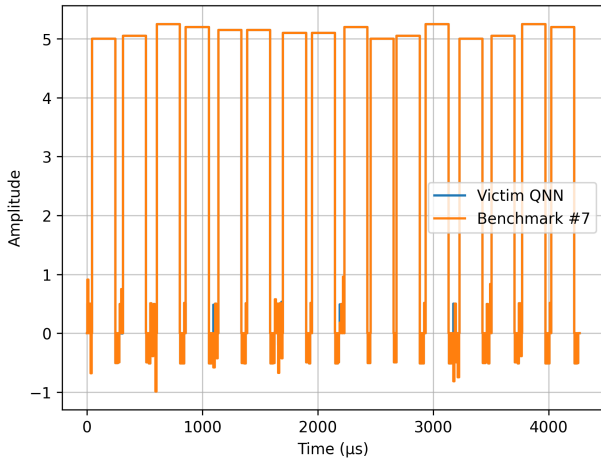


Fig. 13. Power trace comparison: Victim QNN vs. Benchmark Circuit 7

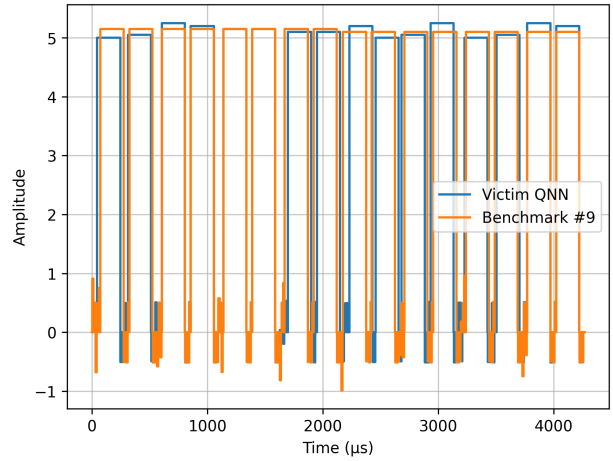
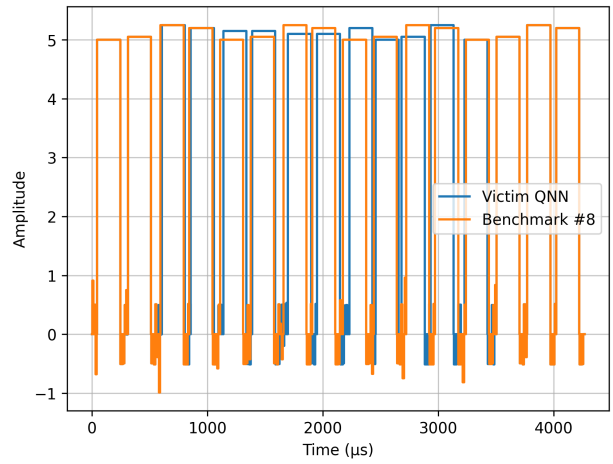


Fig. 14. Power trace comparison of the victim QNN with Benchmark Circuits 8 and 9.

The discrepancy between these plots mainly results from the different entangling patterns visualized in the following plots.

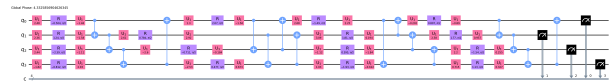


Fig. 15. Benchmark Circuit 7: Entangling pattern  $r = None$ .



Fig. 16. Benchmark Circuit 8: Entangling pattern  $r = 1$ .

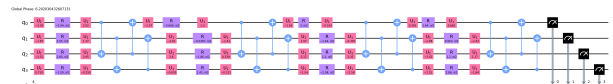


Fig. 17. Benchmark Circuit 9: Entangling pattern  $r = 2$ .

## REFERENCES

- [1] Abdullah Ash-Saki, Mahabubul Alam, and Swaroop Ghosh. “Analysis of crosstalk in NISQ devices and security implications in multi-programming regime”. In: *Proceedings of the ACM/IEEE International Symposium on Low Power Electronics and Design*. New York, NY, USA: Association for Computing Machinery, Aug. 2020, pp. 25–30. ISBN: 978-1-4503-7053-0. URL: <https://doi.org/10.1145/3370748.3406570>.
- [2] Julian Berberich, Daniel Fink, Daniel Pranjić, Christian Tutschku, and Christian Holm. “Training robust and generalizable quantum models”. In: (2023). Version Number: 3. URL: <https://arxiv.org/abs/2311.11871>.
- [3] Navnil Choudhury, Chaithanya Naik Mude, Sanjay Das, Preetham Chandra Tikkireddi, Swamit Tannu, and Kanad Basu. “Crosstalk-induced Side Channel Threats in Multi-Tenant NISQ Computers”. In: (Dec. 2024). arXiv:2412.10507 [cs]. URL: <http://arxiv.org/abs/2412.10507>.
- [4] Pascal Debus, Maximilian Wendlinger, Kilian Tscharke, Daniel Herr, Cedric Brüggemann, Daniel Ohl de Mello, Juris Ulmanis, Alexander Erhard, Arthur Schmidt, and Fabian Petsch. “Entangled Threats: A Unified Kill Chain Model for Quantum Machine Learning Security”. In: (July 2025). URL: <https://arxiv.org/abs/2507.08623>.
- [5] Yuxuan Du, Min-Hsiu Hsieh, Tongliang Liu, Dacheng Tao, and Nana Liu. “Quantum noise protects quantum classifiers against adversaries”. In: *Physical Review Research* 3.2 (May 2021). Publisher: American Physical Society, p. 023153. URL: <https://link.aps.org/doi/10.1103/PhysRevResearch.3.023153>.
- [6] Ferhat Erata, Chuanqi Xu, Ruzica Piskac, and Jakob Szefer. “Quantum Circuit Reconstruction from Power Side-Channel Attacks on Quantum Computer Controllers”. In: *IACR Transactions on Cryptographic Hardware and Embedded Systems* 2024.2 (Mar. 2024), pp. 735–768. URL: <https://tches.iacr.org/index.php/TCHES/article/view/11445>.
- [7] Federal Office for Information Security. *QML-ESA – Advanced Security Analysis of Quantum Machine Learning*. Tech. rep. Federal Office for Information Security (BSI), 2026. URL: [https://www.bsi.bund.de/DE/Service-Navi/Publikationen/Studien/QML/QML\\_node.html](https://www.bsi.bund.de/DE/Service-Navi/Publikationen/Studien/QML/QML_node.html) (visited on 06/08/2026).
- [8] Bhaskar Gaur and Himanshu Thapliyal. “Crosstalk Attack Resilient RNS Quantum Addition”. In: *2025 IEEE International Symposium on Circuits and Systems (IS-CAS)*. 2025, pp. 1–5. URL: <https://arxiv.org/abs/2410.23217>.
- [9] Ian J. Goodfellow, Jonathon Shlens, and Christian Szegedy. “Explaining and Harnessing Adversarial Examples”. In: (Mar. 2015). arXiv:1412.6572. URL: <http://arxiv.org/abs/1412.6572>.
- [10] Benjamin Harper, Behnam Tonekaboni, Bahar Goldozian, Martin Sevier, and Muhammad Usman. “Crosstalk Attacks and Defence in a Shared Quantum Computing Environment”. In: (2024). Version Number: 1. URL: <https://arxiv.org/abs/2402.02753>.
- [11] Andreas Ketterer and Thomas Wellens. “Characterizing Crosstalk of Superconducting Transmon Processors”. In: *Physical Review Applied* 20.3 (2023), p. 034065. URL: <https://arxiv.org/abs/2303.14103>.
- [12] Wei Jie Bryan Lee, Siyi Wang, Suman Dutta, Walid El Maouaki, and Anupam Chattopadhyay. “SWAP Attack: Stealthy Side-Channel Attack on Multi-Tenant Quantum Cloud System”. In: (Feb. 2025). arXiv:2502.10115 [quant-ph]. URL: <http://arxiv.org/abs/2502.10115>.
- [13] Nana Liu and Peter Wittek. “Vulnerability of quantum classification to adversarial perturbations”. In: *Physical Review A* 101.6 (June 2020), p. 062331. ISSN: 2469-9926, 2469-9934. URL: <https://link.aps.org/doi/10.1103/PhysRevA.101.062331>.
- [14] Chao Lu, Esha Telang, Aydin Aysu, and Kanad Basu. “Quantum Leak: Timing Side-Channel Attacks on Cloud-Based Quantum Services”. In: (Jan. 2024). arXiv:2401.01521 [cs]. URL: <http://arxiv.org/abs/2401.01521>.
- [15] Sirui Lu, Lu-Ming Duan, and Dong-Ling Deng. “Quantum adversarial machine learning”. In: *Physical Review Research* 2.3 (Aug. 2020), p. 033212. ISSN: 2643-1564. URL: <https://link.aps.org/doi/10.1103/PhysRevResearch.2.033212>.
- [16] Aleksander Madry, Aleksandar Makelov, Ludwig Schmidt, Dimitris Tsipras, and Adrian Vladu. “Towards Deep Learning Models Resistant to Adversarial Attacks”. In: (Sept. 2019). arXiv:1706.06083. URL: <http://arxiv.org/abs/1706.06083>.
- [17] Prakash Murali, David C. McKay, Margaret Martonosi, and Ali Javadi-Abhari. “Software Mitigation of Crosstalk on Noisy Intermediate-Scale Quantum Computers”. In: *Proceedings of the Twenty-Fifth International Conference on Architectural Support for Programming Languages and Operating Systems*. ASPLOS ’20. Association for Computing Machinery, 2020, pp. 1001–1016. URL: <https://arxiv.org/abs/2001.02826>.
- [18] Adrián P’erez-Salinas, Alba Cervera-Lierta, Elies Gil-Fuster, and Jos’e I. Latorre. “Data re-uploading for a universal quantum classifier”. In: *Quantum* 4 (2020), p. 226. URL: <https://quantum-journal.org/papers/q-2020-02-06-226/>.

- [19] Deepak Ranga, Aryan Rana, Sunil Prajapat, Pankaj Kumar, Kranti Kumar, and Athanasios V. Vasilakos. “Quantum Machine Learning: Exploring the Role of Data Encoding Techniques, Challenges, and Future Directions”. In: *Mathematics* 12.21 (2024), p. 3318. URL: <https://www.mdpi.com/2227-7390/12/21/3318>.
- [20] Wenhui Ren et al. “Experimental quantum adversarial learning with programmable superconducting qubits”. In: *Nature Computational Science* 2.11 (Nov. 2022), pp. 711–717. ISSN: 2662-8457. URL: <https://www.nature.com/articles/s43588-022-00351-9>.
- [21] Suryansh Upadhyay and Swaroop Ghosh. “Quantum Quandaries: Unraveling Encoding Vulnerabilities in Quantum Neural Networks”. In: (Feb. 2025). arXiv:2502.01486 [quant-ph]. URL: <http://arxiv.org/abs/2502.01486>.
- [22] Maximilian Wendlinger, Kilian Tscharke, and Pascal Debus. “A Comparative Analysis of Adversarial Robustness for Quantum and Classical Machine Learning Models”. In: *arXiv.org* (Apr. 2024). URL: <https://arxiv.org/abs/2404.16154v1>.
- [23] Maxwell T. West, Sarah M. Erfani, Christopher Leckie, Martin Sevier, Lloyd C. L. Hollenberg, and Muhammad Usman. “Benchmarking adversarially robust quantum machine learning at scale”. In: *Physical Review Research* 5.2 (June 2023). Publisher: American Physical Society, p. 023186. URL: <https://link.aps.org/doi/10.1103/PhysRevResearch.5.023186>.
- [24] Chuanqi Xu, Ferhat Erata, and Jakub Szefer. “Exploration of Power Side-Channel Vulnerabilities in Quantum Computer Controllers”. In: *Proceedings of the 2023 ACM SIGSAC Conference on Computer and Communications Security*. Copenhagen Denmark: ACM, Nov. 2023, pp. 579–593. ISBN: 9798400700507. URL: <https://dl.acm.org/doi/10.1145/3576915.3623118>.